frontiers | Frontiers in Environmental Science

TYPE Original Research
PUBLISHED 23 August 2022
DOI 10.3389/fenvs.2022.986866

OPEN ACCESS

EDITED BY
Junyuan Guo,
Chengdu University of Information Technology, China

REVIEWED BY
Shuang Luo,
Hunan Agricultural University, China
Guiyin Wang,
Sichuan Agricultural University, China

*CORRESPONDENCE
Yong Wu,
ywu@cdut.edu.cn
Weiguo Tu,
wgtu028@163.com

SPECIALTY SECTION
This article was submitted to Toxicology, Pollution and the Environment, a section of the journal Frontiers in Environmental Science

RECEIVED 05 July 2022
ACCEPTED 19 July 2022
PUBLISHED 23 August 2022

CITATION
Li S, Wu Y, Nie F, Tu W, Li X, Luo X, Luo Y, Fan H and Song T (2022), Remediation of nitrate contaminated groundwater using a simulated PRB system with an La–CTAC–modified biochar filler. *Front. Environ. Sci.* 10:986866. doi: 10.3389/fenvs.2022.986866

Remediation of nitrate contaminated groundwater using a simulated PRB system with an La–CTAC–modified biochar filler

Sen Li[1,2], Yong Wu[1]*, Fuyu Nie[1], Weiguo Tu[2]*, Xueling Li[1], Xuemei Luo[2], Yong Luo[2], Hua Fan[2] and Tao Song[3]

[1]College of Environment and Civil Engineering, Chengdu University of Technology, Chengdu, China, [2]Sichuan Provincial Academy of Natural Resource Sciences, Chengdu, China, [3]School of Environment and Resource, Southwest University of Science and Technology, Mianyang, China

In the present study, the *Erigeron canadensis* L., a typical invasive plant in Southwest China, was utilized as the raw material to prepare original biochar (ECL), a rare earth element La–modified biochar (La–ECL), and a rare earth element La coupling cationic surfactant [cetyltrimethylammonium chloride (CTAC)]–modified biochar (La/CTAC–ECL). These materials were then added to simulated permeable reactive barriers (PRBs) and their nitrate (NO_3^-) contaminant remediation performances were evaluated in groundwater. The results show that the breakthrough time for NO_3^- in a simulated PRB column increases as the concentration of the influent NO_3^- and the flow rate decreases, whereas with the increases of filler particle size and the height of the filler in the column initially increases, and then decreases. Considering an initial NO_3^- concentration of 50 mg L^{-1}, and a filler particle size range of 0.8–1.2 mm, the maximum adsorption capacity of the La/CTAC–ECL column for NO_3^- is 18.99 mg g^{-1} for a filler column height of 10 cm and an influent flow rate of 15 ml min^{-1}. The maximum quantity of adsorbed NO_3^- of 372.80 mg is obtained using a filler column height of 15 cm and an influent flow rate of 10 ml min^{-1}. The Thomas and Yoon–Nelson models accurately predict the breakthrough of NO_3^- in groundwater in the simulated PRB column under different conditions, and the results are consistent with those from dynamic NO_3^- adsorption experiments. TEM, XRD, FTIR, and XPS analyses demonstrate that the modification using the La and CTAC improves the surface structure, porosity, permeability, and configuration of functional groups of the biochar. The mechanisms of NO_3^- removal from groundwater using the La/CTAC–ECL include pore filling, surface adsorption, ion exchange, and electrostatic adsorption. The composite La/CTAC–ECL exhibits a superior potential for the remediation of NO_3^- contaminated groundwater.

KEYWORDS

nitrate, groundwater, biochar composite, permeable reactive barrier, adsorption

1 Introduction

Groundwater is indispensable for daily human activities (Song et al., 2021) and more than 1.5 billion people worldwide rely on it for drinking, especially in developing countries (Shaji et al., 2021), such as China (Jia et al., 2019). However, the quality of groundwater is increasingly degraded in many areas by pollutants from sources such as runoff from agricultural activities, industrial wastewaters, and municipal wastewater treatment systems (Spalding et al., 2019; McDonough et al., 2020; Krimsky et al., 2021; He et al., 2022). Nitrate (NO_3^-) is the most common groundwater pollutant, and its rapid increase in shallow groundwater aquifers is a major concern in many countries (Kim et al., 2019; Taufiq et al., 2019). The long–term consumption of water containing a high concentration of NO_3^- poses a serious threat to human health. It elevates the risk of diseases, such as methemoglobinemia, esophageal cancer, lymphoma, and gastric cancer (Temkin et al., 2019; Stayner et al., 2021; Liu M. et al., 2022). Hence, many countries and organizations have suggested 10 mg L^{-1} as the maximum permissible limit of NO_3^- in drinking water (USEPA, 2012; Anshumala et al., 2021; Zhao et al., 2022). The effective *in situ* remediation of NO_3^- contaminated groundwater is a global issue because of the impact of this pollutant on human activities and the sustainable development of the environment.

Technologies for the *in situ* removal of NO_3^- from groundwater are numerous, but the most commonly employed include the following: biological (Chakraborty et al., 2022), physical (Yang et al., 2019), and electrokinetic remediation (Ghaeminia and Mokhtarani, 2018) as well as the permeable reactive barrier (PRB) (Mittal et al., 2020; Amoako–Nimako et al., 2021). The PRB is gaining increasing attention for groundwater remediation because of its wide applicability, high remediation efficiency, and low cost (Zhao et al., 2022). Mechanisms associated with the removal of pollutants from groundwater using the PRB include the following: reduction (Mittal et al., 2020), fixation (de Repentigny et al., 2018), precipitation (Faisal et al., 2020), and adsorption (Gibert et al., 2019), and these can be divided into the biological, chemical, and physical PRB (Zhao et al., 2022). However, chemical/biological reduction and immobilization techniques for the removal of NO_3^- from groundwater are limited by factors such as the high cost and risk of secondary pollution (Zhao et al., 2022). For example, in chemical PRB technology, reductive denitrification using the zero-valent iron and its associated materials mainly produces NH_3, which causes persistent groundwater pollution due to the presence of NH_4^+–N (Guo et al., 2021). Meanwhile, in biological PRB technology, an insufficient microbial carbon source can promote the accumulation of NO_2^-–N during denitrification (Zhao et al., 2022), whereas excessive carbon can elevate the dissolved organic matter and sludge (Fu et al., 2022). Moreover, because of its high stability and solubility in water, chemical precipitation is unsuitable for the removal of NO_3^- from groundwater (Velusamy et al., 2021). Fortunately, adsorption is widely used for the removal of pollutants from groundwater because the associated methods integrate physical and chemical processes, and these are advantageous because of their simple operation, cost–effectiveness, and environmental friendliness (Dai et al., 2019; Ambaye et al., 2021). Therefore, existing approaches for the removal of NO_3^- by chemical or biological reduction exhibit technical limitations, and a promising strategy to overcome these is to develop high capacity, strong complexation/exchange potential, and environment-friendly adsorbents for use as fillers in the PRB technology.

Owing to their unique physical and chemical properties, biochar is widely utilized in the control of water pollution (Dai et al., 2020; Zhang et al., 2020). However, the surface of a biochar material is often characterized by a high negative potential, and this inhibits its adsorption of anions, such as the NO_3^- in water (Yang et al., 2017). Therefore, the structural characteristics of biochar materials are optimized through physicochemical and biochemical modifications to overcome their poor adsorption of oxygen–containing ions (Zhou et al., 2020; Zheng et al., 2021). According to previous studies, the introduction of metals into a biochar material significantly enhances its anion adsorption capacity (Hasan et al., 2020; Zhang et al., 2020; Lakshmi et al., 2021). For example, loading the surface of a biochar material with La can alter the ion coordination, lower the surface electronegativity, and reduce electrostatic repulsion, and promote its adsorption of oxoacids from water (Wu et al., 2007). Owing to its strong affinity for anions such as PO_4^{3-} and F^-, the higher the loading of La on the surface of a biochar material, the higher the adsorption for these anions (Kong et al., 2019; Li et al., 2020); however, the removal of NO_3^- is relatively low. Conversely, the loading of cationic surfactants on the surface of a biochar material promotes the formation of hydrophilic groups, and these enhance the complexation potential on its surface, thereby improving its ability for the removal of anionic pollutants from water (Shahverdi et al., 2016; Kosaiyakanon and Kungsanant, 2020). Shahverdi et al. (2016) indicated that a poplar biochar modified using a cationic surfactant produced a maximum adsorption capacity of 52.63 mg g^{-1} for Cr(VI) from water. Kosaiyakanon and Kungsanant (2020) reported that the removal efficiency of active yellow 145 from wastewater using a coffee shell biochar modified with a cationic surfactant attained 83.7%. Therefore, the modification of a biochar material using a combination of La and a cationic surfactant can produce a composite material characterized by an enhanced adsorption capacity for NO_3^- from groundwater.

Currently, biochar is prepared from diverse biomass, but this is dominated by bough, straw, and nutshell (Usman et al., 2016; Chandra et al., 2020; Vijayaraghavan and Balasubramanian, 2021). However, owing to structural differences, the pollutant

removal capacities of biochar from different biomass vary (Zhang et al., 2020). Usman et al. (2016) investigated the adsorption potential of pristine and modified biochar prepared using cone fruit waste on NO_3^- in water and reported a capacity of just 1.02 mg g^{-1} for the former. Relatedly, Zhao et al. (2018) compared the performances of biochar prepared using corncob, peanut husk, and cotton stalk for the removal of NO_3^- from water and reported the highest adsorption capacity of 14.46 mg g^{-1} for the corncob–derived biochar. Further, Alsewaileh et al. (2019) indicated that biochar prepared using date palm produced an adsorption capacity of NO_3^- from water of 7.73 mg g^{-1}. Therefore, the adsorption capacity of a biochar material depends on the raw material utilized for its preparation. In recent years, invasive plants are emerging as a major hidden danger that is damaging the regional ecological balance and endangering social development in Southwest China because of their high reproduction and growth adaptability (Yuan et al., 2021). The preparation of biochar using these plants and its utilization for the remediation of NO_3^- polluted groundwater can control their spread and protect the biodiversity in the region (Kumari et al., 2021).

Therefore, in the present study, the *Erigeron canadensis* L., which is a typical invasive plant in Southwest China, was utilized for the preparation of biochar. A biochar composite for the removal of NO_3^- from water was prepared by modifying the prepared biochar using $LaCl_3$ and cetyltrimethylammonium chloride (CTAC). The objectives of the present study were to: 1) investigate the performance of prepared biochar composite for the adsorption of NO_3^- from groundwater and 2) elucidate the adsorption mechanism of the biochar composite when used as a filler in the PRB technology.

2 Materials and methods

2.1 Reagents and groundwater samples

The analytical grade KNO_3, $LaCl_3$ $7H_2O$, CTAC, and HCl utilized in the present study were purchased from the Sinopharm Chemical Reagent Co., Ltd. (Shanghai, China). To ensure that the investigations were representative, NO_3^- contaminated groundwater samples were collected from the same well in a farm in Chengdu, Sichuan Province, China (30°59′22″N, 104°07′20″E). The samples were taken from a depth of 6 m and the volume of each sample was 200 L. These samples were stored in polyethylene bottles at 4°C and used for the investigation of NO_3^- adsorption from contaminated groundwater. Hydrochemical characteristics of these groundwater samples are presented in Supplementary Table S1. Groundwater involving different concentrations of NO_3^- were prepared by weighing and dissolving 0.613 g of KNO_3 in ultrapure water. The volume of the solution was adjusted to 1 L to produce a stock solution with a NO_3^- concentration of 1,000 mg L^{-1}. Approximately 976.56 ml of the collected groundwater with a NO_3^- concentration of 33.47 mg L^{-1} was increased to 1 L by adding ultrapure water to yield a NO_3^- concentration of 25 mg L^{-1}. Relatedly, the collected groundwater was increased to 1 L by adding 25.04 and 76.35 ml of the stock solution to produce contaminated groundwater with NO_3^- concentrations of 50 and 100 mg L^{-1}, respectively.

2.2 Preparation and characterization of biochar composites

2.2.1 Preparation of biochar composites

The *Erigeron canadensis* L. that was used as the raw material to prepare the biochar was obtained from Xinjin County in Sichuan Province (30°23′27″ N and 103°47′18″E). In the laboratory, these plants were washed using distilled water and dried at 65°C. Subsequently, the plants were macerated in a ceramic crucible and then placed in a muffle furnace (SX2–4–10NP, Shanghai Yiheng Technology Co., Ltd., Shanghai, China). The air in the muffle furnace was purged using N_2, and then the temperature of the furnace was raised to 600°C at a heating rate of 10°C min^{-1}, and then held isothermally for 2 h. The solid product was then washed using ultrapure water until the supernatant was neutral and then dried at 65°C. The solids were then ground to pass through a 200–mesh sieve to produce the pristine *Erigeron canadensis* L. biochar (ECL).

The La– and La/CTAC–modified biochar composites were prepared following the method of Luo et al. (2020), and this involved the combination of a simple co–precipitation and an organic modification method. Approximately 5 g of the ECL was added to 50 ml of a solution containing 1.0 mol L^{-1} of $LaCl_3$ and the mixture was shaken for 6 h. This was followed by a dropwise addition of 0.5 mol L^{-1} of NaOH to produce a solution with a pH of 11.5, and this caused precipitation of La^{3+}. The mixture was continuously stirred at 25°C using a magnetic stirrer for 24 h, and then the solid material was recovered and rinsed with ultrapure water and alcohol until these were free of chloride. Finally, the solid material was dried in an LGJ–10 vacuum freeze dryer (Beijing Songyuanhuaxing Technologies, Beijing, China) for 48 h and then ground to particles passing through a 200–mesh sieve to produce the La–modified biochar (La–ECL).

Additionally, approximately 5 g of the La–ECL was added to a 50–ml solution containing 0.05 mol L^{-1} of CTAC, and the mixture was shaken at room temperature with a speed of 150 rpm for 24 h. The solid material was then collected and rinsed using ultrapure water and alcohol until it was free of chloride. The solid material was also dried in an LGJ–10 vacuum freeze dryer for 48 h and then ground to particles passing through a 200–mesh sieve to produce the La/CTAC–modified biochar (La/CTAC–ECL). In addition, biochar granules were

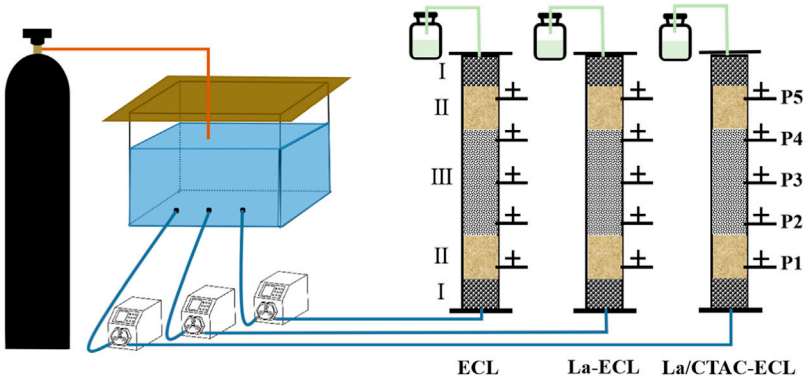

FIGURE 1
Diagram showing simulated PRB columns utilized for the dynamic adsorption of NO_3^- from groundwater.

prepared using a laboratory–scale drum rotation granulator (CQM10, Qingdao Co–nele Machinery Co., Ltd., Qingdao, China), and the particle sizes involved the ranges of 0.25–0.5, 0.8–1.2, and 1.8–2.2 mm. To ensure that the biochar granules satisfied the strength and particle size requirements, 2% cement–based adhesive was added as a binder during the granulation process.

2.2.2 Characterization of the biochar materials

The ECL, La–ECL, and La/CTAC–ECL were analyzed to evaluate their quality, determine their properties, and highlight the associated mechanisms in the removal of NO_3^- from polluted groundwater. The surface morphologies and element distributions in the ECL, La–ECL, and La/CTAC–ECL were characterized before and after the NO_3^- removal experiments using a scanning electron microscope (Hitachi Flex SEM 1000, Japan) with an operating voltage of 5 kV and by transmission electron microscopy and energy dispersive spectroscopy performed using a JEM2100 instrument (JEOL, Tokyo, Japan) with an accelerating voltage of 200 kV. The Brunauer–Emmett–Teller specific surface areas of the materials were determined by performing N_2 adsorption–desorption tests at 77 K using a Microtrac BEL high–resolution gas adsorption analyzer (Microtrac, Montgomeryville, PA, United States). The thermal stabilities of the materials were assessed using a TGA5500 thermogravimetric analyzer (TA Instruments, New Castle, DE, United States). The crystal structures of the materials were also analyzed using an X–ray diffractometer with Cu Kα radiation at a voltage of 40 kV and a current of 30 mA (Rigaku D/MAX 2500V/PC, Japan) that was operated at a scan rate of 8 min^{-1} from 5° to 80° (2θ). A Fourier transform infrared spectrometer (Nicolet 5700 FT–IR Spectrometer, America) with the potassium bromide (KBr) tableting method was used to evaluate changes in functional groups and chemical bonds before and after usage of the materials, and the absorption range was 4,000–400 cm^{-1}, whereas the frequency was 4 cm^{-1}. The surface compositions of the materials were determined with an Escalab 250Xi X–ray photoelectron spectrometer equipped with a monochromatic Al Kα X–ray source (Thermo Fisher, MA, United States). The wide spectra were recorded from an energy range of 0–1,400 eV on 10 scans, in which the pass energy was 50 eV and the step size was 0.05 eV. The binding energies for the sample XPS spectra were adjusted by setting C to 1 s at 284.6 eV.

2.3 Design and operation of the simulated PRB system

2.3.1 Simulated PRB column design

The simulated PRB column involved a polyethylene material (Figure 1) measuring 25 cm in height, 2 cm in the internal diameter, 3 cm in external diameter, and 0.5 cm in wall thickness. The PRB column was divided into segments I, II, and III. Segment part I was filled with glass beads measuring 2.5 mm in size, up to a height of 2 cm, and these mainly served for filtration, buffering, and protection. Segment II was filled with quartz sand particles with a size range of 0.8–1.2 mm, up to a height of 3 cm, to simulate an aquifer. Segment III represented the adsorption layer and its height was 5–15 cm, and this was filled with the pristine or modified biochar. Five sampling outlets at intervals of 5 cm were created at the side of the PRB simulation column, and these were numbered P1–P5 from the bottom to the top. The quartz sand and glass beads used in the experiments were initially washed using tap water, and subsequently soaked in a 5% HCl solution for 12 h, and then finally washed using ultrapure water and dried.

Three peristaltic pumps (KSP–F01A, Kamoer Fluid Tech Co., Ltd., Shanghai) were used to supply water from the lower ends of three PRB simulation columns that were operated

simultaneously. In column 1, the ECL was used as the filler, whereas column 2 contained the La–ECL, and in column 3, the La/CTAC–ECL was utilized.

2.3.2 Simulated PRB column dynamic adsorption experiment

Experiments were conducted using different initial concentrations of NO_3^-, influent flow rate, filler particle size, and filler height to evaluate the effects of these factors on the adsorption of NO_3^- from groundwater by the pristine and modified biochar materials. The NO_3^- concentration was determined by gas-phase molecular absorption spectrometry.

1) The effect of the initial concentration of NO_3^- was assessed by performing experiments involving concentrations of 25, 50, and 100 mg L^{-1}. The influent flow rate, filler particle size range, and column height were fixed at 10 ml min^{-1}, 0.8–1.2 mm, and 10 cm, respectively.
2) The influence of the influent flow rate was assessed using flow rates of 5, 10, and 15 ml min^{-1}. In these experiments, the initial concentration of NO_3^-, filler particle size range, column height was correspondingly maintained at 50 mg L^{-1}, 0.8–1.2 mm, and 10 cm.
3) The effect of the filler particle size was investigated by conducting experiments involving size ranges of 0.25–0.5, 0.8–1.2, and 1.8–2.2 mm. In the experiments, the initial concentration of NO_3^-, influent flow rate, and column height were preserved at 50 mg L^{-1}, 10 ml min^{-1}, and 10 cm, respectively.
4) The impact of the filler thickness was investigated using column heights of 5, 10, and 15 cm. The initial concentration of NO_3^-, influent flow rate, and filler particle size range were retained at 50 mg L^{-1}, 10 ml min^{-1}, and 0.8–1.2 mm, respectively.

2.3.3 Determination of porosity and permeability

The porosity was measured by reversing the flow direction of the peristaltic pump after the dynamic adsorption experiment of the PRB simulation column was completed. The water left in the PRB simulation column was then removed as much as possible, and the water volume was V. The porosity (η) was the calculated according to the following expression:

$$\eta = \frac{V}{V_0} \tag{1}$$

where V (cm^3) is the volume of water left in the column and V_0 (cm^3) is the volume of PRB column at the height of the filler.

The permeability of the PRB filler before and after each experiment was determined using the constant pressure method, and the device utilized is shown in Supplementary Figure S1. Two identical pipette tubes were connected to sampling holes P1 and P5, and tap water was then supplied to the PRB column from the bottom to the top at a constant flow rate of 10 ml min^{-1}. This created a head difference between the two pipettes, and following the stabilization of the head difference and seepage water, the water output (V) through the filler per unit time (t) was measured. The permeability (K) was then calculated according to the following expression:

$$K = \frac{V\Delta L}{\Delta H A t} \tag{2}$$

In Eq. 2, V (cm^3) represents the volume of water flowing from the outlet at time t, $\triangle L$ (16 cm) is the difference in height between the two pressure measuring tubes, $\triangle H$ (cm) denotes the head difference between sampling holes P1 and P5, A (19.625 cm^2) represents the cross–sectional area of the simulated PRB column, and t (s) is the time required for the liquid level differential pressure gauge to stabilize.

2.4 Penetration curve model fitting

The breakthrough curve is an important component of the dynamic column experiment. It enables the characterization of the adsorption of the adsorbate on the filler in the dynamic PRB column under the specified conditions. The Thomas model is mainly utilized to determine the adsorption capacity of the adsorbent, whereas the Yoon–Nelson model is primarily used to predict the removal efficiency of the dynamic PRB column. Therefore, the Thomas and Yoon–Nelson models were selected for the fitting of the adsorption in the PRB column in the present study. These models can be represented using the following expressions:

$$\text{Thomas model: } \frac{Ct}{C0} = \frac{1}{1 + \exp\left[\frac{k\text{Th}}{Q}(q \times \text{m} - C0 \times V)\right]} \tag{3}$$

$$\text{Yoon} - \text{Nelson model: } \frac{Ct}{C0} = \frac{1}{1 + \frac{1}{\exp(k\text{YN} \times t - k\text{YN} \times \tau)}} \tag{4}$$

where C_t (mg L^{-1}) is the concentration of NO_3^- at the water outlet at a time t, C_0 (mg L^{-1}) represents the concentration of NO_3^- at the water inlet, k_{Th} (ml min^{-1} cm^{-1}) denotes the Thomas rate constant, Q (ml min^{-1}) stands for the influent flow rate, q (mg g^{-1}) is the adsorption capacity of the filler in the PRB column at the adsorption equilibrium, m is the mass of the filler in the PRB column, V (ml) is the volume of simulated NO_3^- contaminated groundwater that is passing through the PRB column, k_{YN} is the Yoon–Nelson model constant, and τ (h) is the time required for the adsorption value associated with the filler in the PRB column to reach 50% of the total.

3 Results and discussion

3.1 Characterization of biochar composites

The SEM images and EDS element diagrams of ECL, La–ECL, and La/CTAC–ECL were shown in Figure 2. The ECL had a rough surface with some large and dense pores.

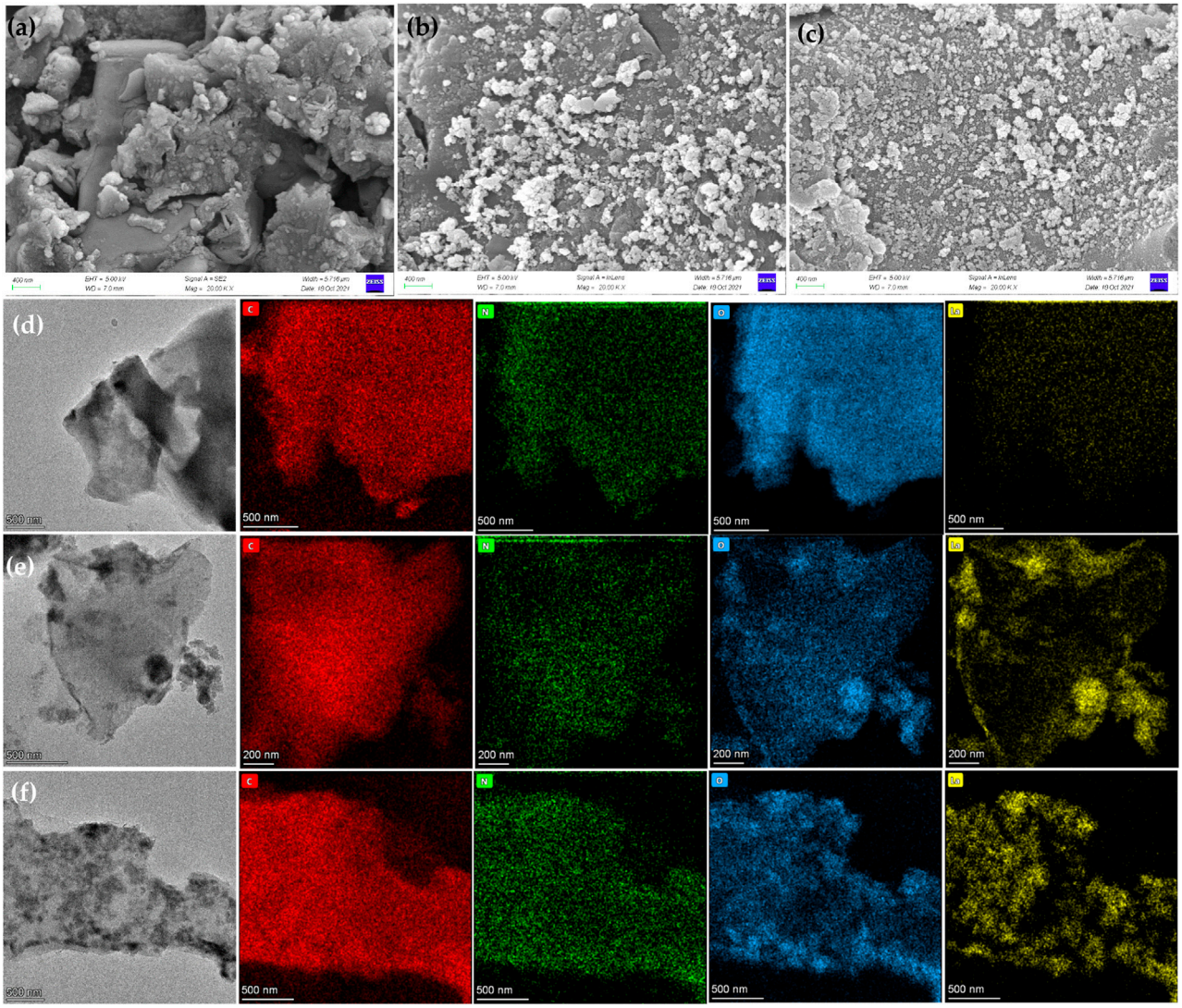

FIGURE 2
SEM analysis of ECL **(A)**, La–ECL **(B)**, and La/CTAC–ECL **(C)**. TEM-mapping and the corresponding EDS mappings of C, N, O, and La on ECL **(D)**, La–ECL **(E)**, and La/CTAC–ECL **(F)**.

Some small aggregated flower–like particulates were attached to the surface of La–ECL and La/CTAC–ECL, which presented that La had been successfully loaded onto the surface of La–ECL and La/CTAC–ECL (Qu et al., 2020). Such structures could supply adequate active sites for the NO_3^- capture (Wang et al., 2016). The EDS spectrograms in Figures 2E,F also confirmed that La was well dispersed onto the surface of La–ECL and La/CTAC–ECL. The BET specific surface area of La–ECL and La/CTAC–ECL was 12.00 and 8.71 $m^2\ g^{-1}$, respectively, which was significantly higher than that of ECL (4.37 $m^2\ g^{-1}$) (Supplementary Table S2). The increase in the specific surface area due to the loading of La dedicated more multiple binding sites and could further enhance the NO_3^- adsorption.

The major weight loss for ECL, La–ECL, and La/CTAC–ECL occurring from ~550 to ~690°C is because of thermal decompositions (Figure 3A). The XRD pattern showed that a broad peak at 2θ value of 29.4, 39.5 and 48.6 appeared on the surface of ECL (Figure 3B), which was a typical characteristic peak of $CaCO_3$. After modification, the load of La on the surface of La–ECL and La/CTAC–ECL predominantly existed in the form of $La(OH)_3$ and La_2O_3 (Zhi et al., 2022). The XPS also was consistent with EDS and XRD, which proved that La successfully loaded.

To further explore the surface functional groups, FT–IR spectra of ECL, La–ECL, and La/CTAC–ECL were summarized in Figure 3C. All materials had a broad peak at

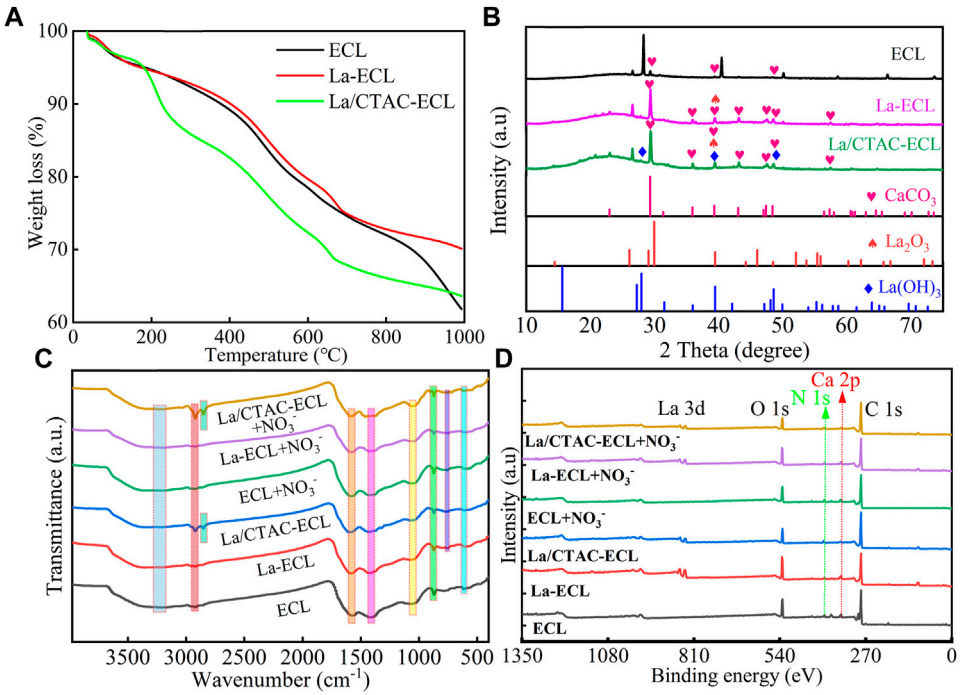

FIGURE 3
TGA curves of ECL, La–ECL, and La/CTAC–ECL **(A)**. XRD **(B)**, FTIR **(C)**, and XPS **(D)** spectra of ECL, La–ECL, and La/CTAC–ECL before and after NO_3^- adsorption **(D)**.

3,201–3,340 cm^{-1}, attributing to the stretching vibrations of O–H stretching vibration in $La(OH)_3$ or surface–adsorbed water molecules. The peak at 2,923 cm^{-1} was attributed to the stretching vibration of $–CH_2$. In addition, two extra peaks at nearby 1,585 and 1,423 cm^{-1} assigned to the C–O stretching, C=C, and C=O bonds in biochar. The strong feature peak at 872 and 615 cm^{-1} was attributed to metallic oxide (M–O) in biochar (Li et al., 2020). In particular, a new peak at 757 cm^{-1} in the La–ECL and La/CTAC–ECL s ascribed to the La–O stretching bond (Wang et al., 2016; Teng et al., 2022).

3.2 Dynamic adsorption of NO_3^- in groundwater

3.2.1 Effect of the influent NO_3^- initial concentration on the dynamic adsorption

As shown in Figure 4, the adsorption capacity and total amount of NO_3^- adsorbed from groundwater in PRB columns of different fillers increase as the influent NO_3^- concentration increase. In the same PRB column, as the initial concentration of NO_3^- in the influent increases, the adsorption amount of NO_3^- from groundwater in the column also increases. However, the lack of multiplied increase indicates that the adsorption of PRB column has a certain saturation. Therefore, the increase in the NO_3^- concentration likely enhances the adsorption or exchange sites of inorganic anions in the PRB column. It may be that the higher concentration of NO_3^- enhances the driving force to surmount the mass transfer resistance between water and biochar material (Aytas et al., 2009), thus improving the contact probability between adsorbate and biochar surface (Qiu et al., 2021). Therefore, the NO_3^- is easier to combine with the adsorption site. Relatedly, the adsorption of NO_3^- from groundwater for PRB columns of different fillers significantly differs for an identical initial concentration. The adsorption breakthrough volume, saturation volume, total adsorbed, and the adsorption capacity for NO_3^- from the studied contaminated groundwater produced the following order for the filler materials: La/CTAC–ECL > La–ECL > ECL.

Regarding the NO_3^- concentrations of 25, 50, and 100 mg L^{-1} in the influent, the NO_3^- adsorption breakthrough volumes of the La/CTAC–ECL–filled column are 7,400, 4,000, and 2000 ml, respectively, whereas the saturation volumes are correspondingly 132,000, 7,200, and 4,000 ml (Supplementary Table S3). Relatedly, the total NO_3^- adsorbed values are 246.25, 269.40, and 286.80 mg, respectively, whereas the corresponding adsorption capacities are 12.32, 13.48, and 14.35 mg g^{-1} (Supplementary Table S3). Obviously, the adsorption capacity of La/CTAC–ECL–filled column for NO_3^- in groundwater significantly exceeds that of the ECL–filled column, which

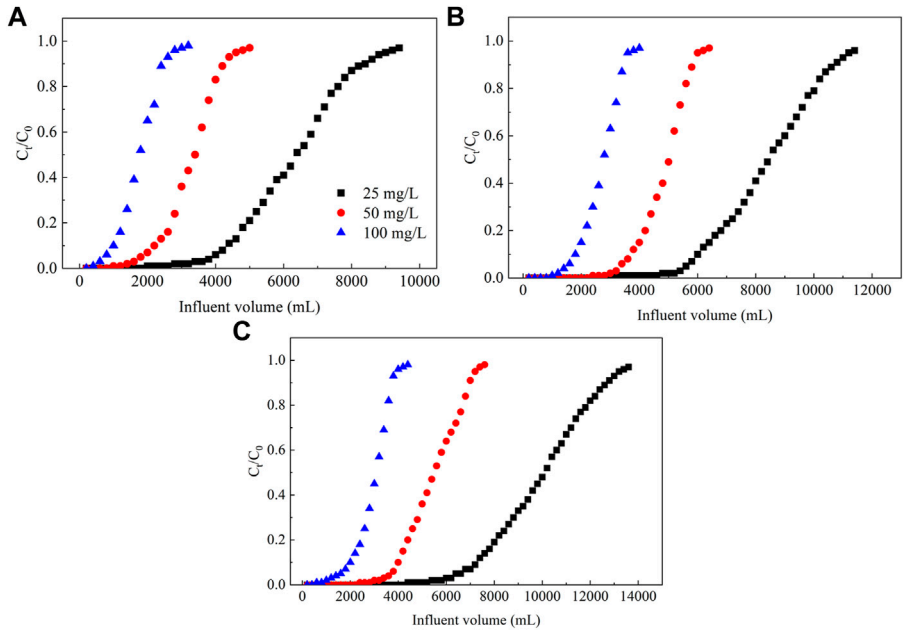

FIGURE 4
Plot showing the effect of the concentration of NO_3^- in the influent on the dynamic adsorption of NO_3^- from groundwater. Note: **(A–C)** represent ECL, La–ECL, and La/CTAC–ECL, respectively.

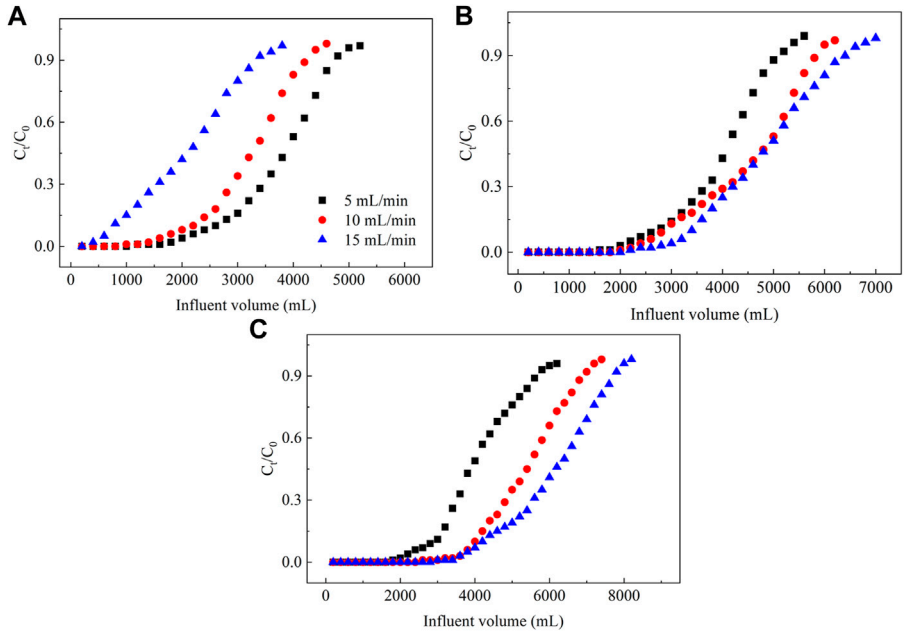

FIGURE 5
Plot showing the effect of the influent flow rate on the dynamic adsorption of NO_3^- from groundwater. Note: **(A–C)** represent ECL, La–ECL, and La/CTAC–ECL, respectively.

suggests that in the La–modified biochar, binding, exchange, and adsorption sites for inorganic anions are likely enhanced via the formation of La^{3+} complexes (Kong et al., 2019; Li et al., 2020). Compared with the La–ECL–filled column, the La/CTAC–ECL–filled column displays a higher NO_3^- adsorption efficiency and capacity. These results indicate that the positive charges associated with the CTAC reduce the electronegativity on the surface of the biochar, lower the electrostatic repulsion, and promote the electrostatic adsorption of the NO_3^- (Fu et al., 2021).

3.2.2 Effect of the influent flow rate on the NO_3^- removal

As shown in Figure 5, as the flow rate of the influent increases, the NO_3^- adsorption breakthrough point for a PRB column decreases and the saturation point lags. The total NO_3^- adsorbed and the adsorption capacities of different PRB columns vary as the inlet flow rate increases. In general, the adsorption capacity of adsorbent often decreases when flow rate increases because of the insufficient residence time between adsorbent and adsorbate (Vilvanathan and Shanthakumar, 2017). However, the adsorption of NO_3^- in groundwater on the column filled with the ECL is best at an influent flow rate of 5 ml min^{-1}, and the total NO_3^- adsorbed and the capacity are 184.90 mg and 9.25 mg g^{-1}, respectively (Supplementary Table S3). Under different influent flow rates, the performance of the columns containing the La–ECL and La/CTAC–ECL for the adsorption of NO_3^- significantly differ from that of the ECL–filled column. The total NO_3^- adsorbed in columns filled with the La–ECL and La/CTAC–ECL at a flow rate of 15 ml min^{-1} was 239.20 and 303.90 mg, respectively, whereas the corresponding adsorption capacities are 11.97 and 15.21 mg g^{-1}, and these values are higher than those associated with other flow rates (Supplementary Table S3).

These results are consistent with those obtained for the removal of Cd^{2+} using an adsorbent prepared from animal bones by Lim and Aris (2014). Their adsorbent exhibited lower effectiveness at wastewater flow rates of 10, 15, and 20 ml min^{-1}, and the corresponding adsorption capacities for Cd^{2+} were 17.7, 41.6, and 66.2 mg g^{-1}. Therefore, a high influent velocity probably impacts the structure of the modified biochar by enhancing ion exchange sites (Setshedi et al., 2014). Alternatively, owing to the reduced electronegativity on the surface of the modified biochar, the affinity for anions is improved (Yang et al., 2017). Considering that the adsorption of NO_3^- on the modified biochar is faster compared to that on the original biochar, a high adsorption capacity can be retained in the former as the flow rate increases.

3.2.3 Effect of the particle size of the filler on NO_3^- removal

The effects of the particle size of the filler on the dynamic adsorption of NO_3^- from groundwater in PRB columns are shown in Figure 6. In a PRB column, considering particle sizes of 0.25–0.5 and 0.8–1.2 mm for the filler, the adsorption breakthrough and saturation points for NO_3^- increase as the particle size range increases for all three PRB column heights, and the slope of the dynamic adsorption curve decreases. However, if the particle size range of the filler increases from 0.8 to 1.2 to 1.8–2.2 mm, the adsorption breakthrough and saturation points of NO_3^- for the three PRB columns are associated with the lower particle size range, and the slope of the dynamic curve increases, thus yielding the shortest NO_3^- breakthrough times. Regarding the particle size ranges of 0.25–0.5, 0.8–1.2, and 1.8–2.2 mm for the filler, the maximum NO_3^- adsorption capacities for the ECL–filled column are 7.56, 8.67, and 7.06 mg g^{-1}, whereas those for the La–ECL–filled column are correspondingly 10.35, 11.46, and 8.23 mg g^{-1}, and those for the column filled with the La/CTAC–ECL are 11.70, 13.68, and 9.61 mg g^{-1}, respectively (Supplementary Table S3).

These results demonstrate that as the particle size of the filler in the PRB column increases, the adsorption capacity values of the pristine and modified biochar materials initially increase, and then decrease. This characteristic is attributed to the low specific surface areas of the filling materials because of the large particles (Li et al., 2019). This decreases the NO_3^- adsorption sites in the PRB column, which is not conducive to the removal of NO_3^- from groundwater using the pristine and modified biochar materials (Yan et al., 2020). In contrast, the biochar materials involving smaller particles are characterized by higher specific surface areas and total pore volumes, which facilitate the penetration of NO_3^- into structure, and thereby produces high adsorption capacities (Liu D. et al., 2022). However, if the particle sizes of the biochar material are very fine, the porosity and permeability of the PRB column are reduced, and these changes decrease the NO_3^- adsorption capacity (Haque et al., 2021). These results demonstrate the importance of the particle size of the filler on the adsorption efficiency and capacity of the PRB column (Gupta and Kua, 2019). Therefore, the pristine and modified biochar materials with a particle size range of 0.8–1.2 mm emerged as the adequate filler material sizes for the PRB column in the present study.

3.2.4 Effect of the height of the filler in the PRB column on NO_3^- removal

As shown in Figure 7, the slope and breakthrough point for the removal of NO_3^- from groundwater depends on the height of the filler in the PRB column. The breakthrough and saturation points for the NO_3^- adsorption on different PRB columns decreases as the height of the filler increases, whereas the total NO_3^- adsorbed and the adsorption capacity gradually increase. As the height of the filler in the PRB column increases from 5 to 15 cm, the volume associated with the NO_3^- breakthrough point for the columns filled with the ECL, La–ECL, and La/CTAC–ECL increases by 333, 250, and 229%, respectively (Supplementary Table S3). Relatedly, the volume linked to the adsorption

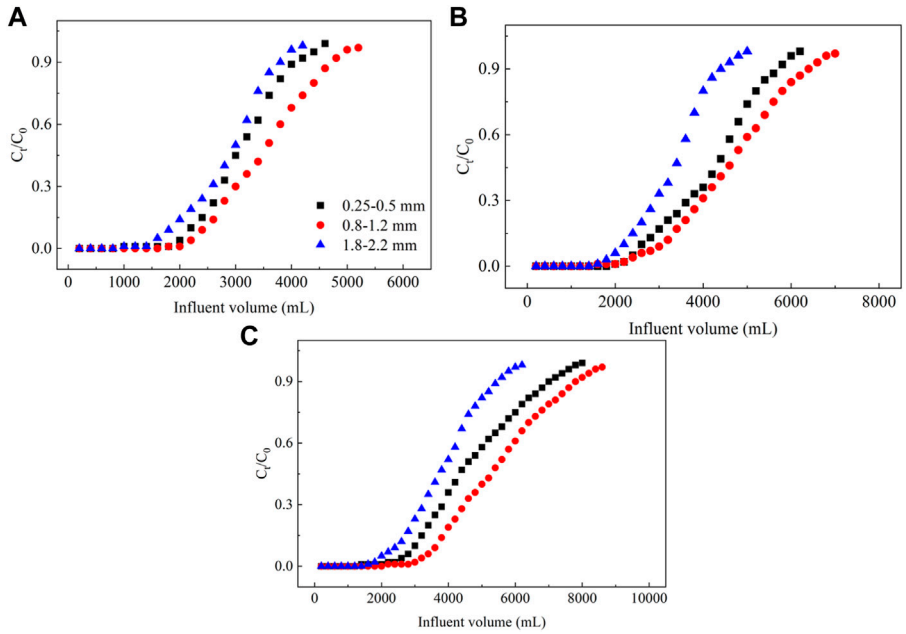

FIGURE 6
Plot showing the effect of the particle size of the filler on adsorption of NO_3^- from groundwater. Note: **(A–C)** represent ECL, La–ECL, and La/CTAC–ECL, respectively.

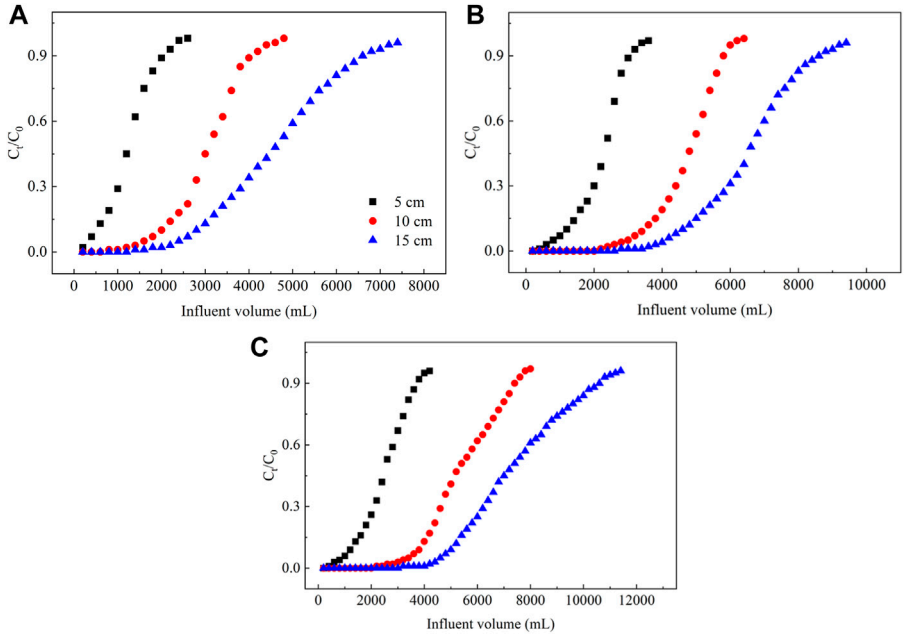

FIGURE 7
Plot showing the effect of the column height of the filler in the PRB on the dynamic adsorption of NO_3^- in groundwater. Note: **(A–C)** represent ECL, La–ECL, and La/CTAC–ECL, respectively.

saturation point increases correspondingly by 192, 159, and 165%, and the total adsorption is elevated by 289, 205, and 205%, respectively. These results demonstrate that the height of the filler in the PRB column significantly affects the adsorption of NO_3^- from groundwater on the column. This behavior is attributed to the larger the mass of filler in the column as the height of the filler increases, thereby augmenting the filler surface area and the number of active binding sites available for NO_3^- adsorption (Ramírez–Rodríguez et al., 2021). Consequently, the reaction time between the NO_3^- and biochar materials in the PRB column is longer, and thus, diffusion into the adsorbent is deeper.

In addition, the higher filling material in the PRB column enhances the overall active sites for adsorption, thereby also improving the efficiency of the column for the adsorption of NO_3^- from groundwater. However, if the height of the filler in the PRB column changes from 5 to 10 cm, the adsorption capacity of the columns filled with the ECL, La–ECL, and La/CTAC–ECL columns for NO_3^- from groundwater increase by 26.96, 8.99, and 11.22%, respectively. Conversely, if the height of the filler in the PRB column increases from 10 to 15 cm, the adsorption capacity for NO_3^- of the columns containing the La–ECL, and La/CTAC–ECL correspondingly decrease by 6.67 and 8.19%. A similar research results was observed by Zhang et al. (2017). They found that the Cd adsorption capacity onto eggshells were 1.13 mg g^{-1} at the filler column height of 10 cm, 1.85 mg g^{-1} at 20 cm, and 1.63 mg g^{-1} at 30 cm. Obviously, the adsorption capacity of the pristine and modified biochar materials for NO_3^- initially increase, and then decrease, as the height of the filler in the PRB column increases. Therefore, in the present study, 10 cm emerged as the optimum height of the filler in the PRB column for the removal of NO_3^- from groundwater.

3.3 Changes in the porosity and permeability coefficient of the filler in the PRB column

The porosity highlights the spatial blockage and resistance to the flow of water within the filler, whereas the permeability coefficient of the PRB column mainly reflects penetration ability of the filling material. The data in Supplementary Table S4 show that the porosity and permeability coefficient of fillers in all PRB columns decrease significantly after the adsorption experiments. The decrease in porosity produces a range of 12.43–27.41%, whereas that of the permeability coefficient is 39.53–68.42%. The maximum decrease in porosity and permeability coefficient is associated with the ECL–filled column. These results demonstrate that the PRB columns containing the fillers are suitable for the adsorption of NO_3^- and other adsorbates from groundwater, but the surfaces of the modified biochar materials are characterized by better pore structures than the pristine biochar. The porosity and permeability coefficient of the biochar materials decrease because of the adsorption of pollutants, such as NO_3^-, in their pore structures and surfaces (Zhang et al., 2020). Alternatively, these decreases may be caused by the adherence of fine particles and microorganisms that are present in the groundwater on surfaces of biochar materials in the PRB column (Mahendra et al., 2015; Gao et al., 2021).

3.4 Penetration curve model fitting

3.4.1 Thomas model

The fitting results based on the Thomas model presented in Table 1 are similar to those of the dynamic adsorption experiments. As the NO_3^- concentration in the influent increases from 50 to 100 mg L^{-1}, the k_{Th} values for the three PRB columns decrease, whereas the q values increase. These changes are attributed to the increase in the concentration of NO_3^- because the occupation of more active sites on the surface of the filler enhances the adsorption saturation capacity (Qiu et al., 2021). The k_{Th} and q values for the ECL–filled column decrease as the flow rate of the influent increases, whereas those for the columns filled with the La–ECL and La/CTAC–ECL increase gradually. These differences are associated with the stronger affinity for NO_3^- and higher ion exchange sites of the modified biochar materials (Li et al., 2020). The k_{Th} and q values for the three PRB columns initially increase, and then decrease, as the particle size range of the filler increases. These changes are linked to the porosity reduction by fine filler particles and the low specific surface area of large particles (Li et al., 2019), which are both unfavorable for the removal of NO_3^- from groundwater.

The k_{Th} and q values also initially increase for the three PRB columns, and then decrease, as the height of the filler in the PRB column increases, and the values associated with varying heights differ significantly. These differences are linked to the increased hydraulic retention in the PRB column as the height of the filler increases, and thus, active sites for the adsorption of NO_3^- are enhanced accordingly. In addition, the R^2 values of the fitting using the Thomas model for all groups of variables exceed 0.98, and these indicate that the model adequately fits the process and it is highly reflective of the dynamic adsorption of NO_3^- in groundwater on the pristine and modified biochar materials (Golie and Upadhyayula, 2016).

3.4.2 Yoon–Nelson model

Data for the k_{YN} and τ that were obtained from fitting using the Yoon–Nelson model are presented in Table 1. As the initial concentration of NO_3^- in the influent and the influent flow rate increase, the k_{YN} values for the three PRB columns also gradually increase, whereas the time τ for filler in the PRB column to produce 50% of the total adsorption gradually decreases. These results indicate that the driving force of the mass transfer in the groundwater increases as the initial concentration of NO_3^- and

TABLE 1 Plot displaying the fitting parameters based on the Thomas and Yoon–Nelson models for dynamic adsorption of NO_3^- in groundwater on the PRB column.

Impact factor		PRB filler	Thomas model			Yoon–Nelson model		
			Q (mg g^{-1})	k_{Th} (ml min^{-1} cm^{-1})	$R2$	T (h)	k_{YN} (min^{-1})	$R2$
Initial concentration of influent NO_3^- (mg L^{-1})	25	ECL	7.92	0.02569	0.9987	10.55	38.54	0.9987
	50		8.32	0.02583	0.9984	5.54	77.49	0.9984
	100		8.89	0.01710	0.9980	2.96	102.59	0.9980
	25	La–ECL	10.57	0.02190	0.9983	14.08	32.84	0.9983
	50		12.32	0.02486	0.9970	8.20	74.59	0.9970
	100		13.73	0.01526	0.9973	4.57	91.58	0.9973
	25	La/CTAC–ECL	12.54	0.01867	0.9988	16.70	28.00	0.9988
	50		13.81	0.01622	0.9961	9.20	48.66	0.9961
	100		15.20	0.01507	0.9956	5.06	90.45	0.9956
Influent flow rate (ml min^{-1})	5	ECL	9.70	0.01216	0.9944	12.92	36.49	0.9944
	10		8.29	0.02570	0.9971	5.52	77.10	0.9971
	15		5.42	0.02949	0.9933	2.41	88.47	0.9933
	5	La–ECL	10.21	0.01147	0.9961	13.59	34.42	0.9961
	10		11.76	0.01678	0.9848	7.83	50.33	0.9848
	15		12.28	0.02525	0.9978	5.45	75.75	0.9978
	5	La/CTAC–ECL	10.30	0.00913	0.9960	13.72	27.38	0.9960
	10		13.76	0.01747	0.9975	9.16	52.42	0.9975
	15		15.69	0.02230	0.9946	6.97	66.90	0.9946
Filler particle size (mm)	0.25–0.5	ECL	7.81	0.02821	0.9985	5.23	84.62	0.9985
	0.8–1.2		8.93	0.02219	0.9967	5.94	66.58	0.9967
	1.8–2.2		7.41	0.02781	0.9961	4.89	83.44	0.9961
	0.25–0.5	La–ECL	10.72	0.01745	0.9950	7.17	52.36	0.9950
	0.8–1.2		11.77	0.01533	0.9987	7.84	45.99	0.9987
	1.8–2.2		8.55	0.24190	0.9975	5.63	72.58	0.9975
	0.25–0.5	La/CTAC–ECL	11.82	0.01254	0.9927	7.91	37.63	0.9927
	0.8–1.2		13.85	0.01206	0.9950	9.22	36.18	0.9950
	1.8–2.2		9.87	0.01739	0.9984	6.51	52.18	0.9984
PRB filler height (cm)	5	ECL	6.33	0.03672	0.9988	2.11	110.17	0.9988
	10		7.79	0.02614	0.9986	5.19	78.42	0.9986
	15		7.78	0.01352	0.9986	7.78	40.57	0.9986
	5	La–ECL	11.47	0.02990	0.9931	3.82	89.72	0.9931
	10		12.10	0.02251	0.9960	8.06	67.52	0.9960
	15		11.10	0.01371	0.9993	11.08	41.13	0.9993
	5	La/CTAC–ECL	12.85	0.02144	0.9988	4.28	64.31	0.9988
	10		13.80	0.01342	0.9938	9.19	40.27	0.9938
	15		12.52	0.00928	0.9942	12.50	27.83	0.9942

inflow flow rate increase, and this accelerates the adsorption of NO_3^- on the adsorbent in the PRB column and hastens the emergence of the adsorption saturation point (Gizaw et al., 2022).

Relatedly, as the particle size of the filler increases, the k_{YN} values for the three PRB columns initially decrease, and then increase, whereas the τ values increase at first, and then decrease. These results demonstrate that as the particle size of each material increases, the permeability and fluid penetration velocity increase, whereas the penetration time reduces. Regarding the increase in height of the filler in the PRB column, the k_{YN} values for the three PRB columns gradually decrease, whereas those for τ increase. These results show that under constant loading, active sites for the adsorption of NO_3^- in the PRB column increase as the height of the filler increases. This characteristic prolongs the breakthrough and adsorption saturation times of NO_3^- in the PRB column. Moreover, by

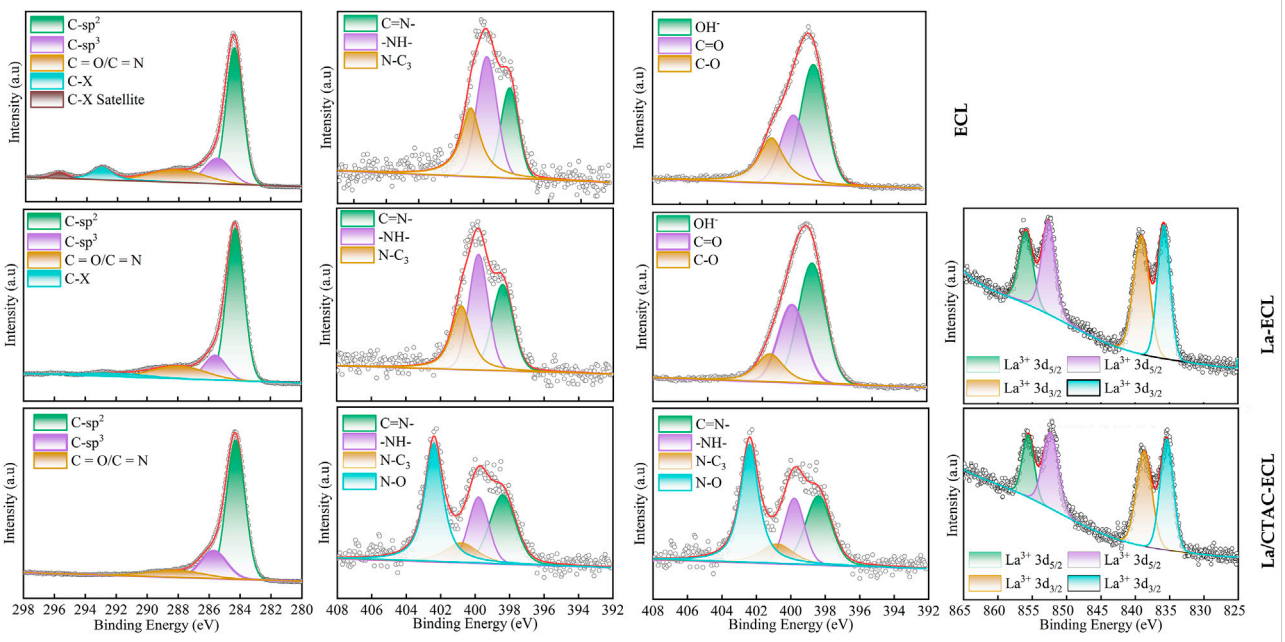

FIGURE 8
C 1 s spectrum, N 1 s spectrum, O 1 s spectrum, and La 3 d spectra of ECL, La–ECL, and La/CTAC–ECL after NO_3^- adsorption.

comparing the fitting parameters of the Yoon–Nelson model with results from the dynamic adsorption experiments, the τ values for all groups of variables are similar, and the associated R^2 values exceed 0.98. These results demonstrate that the Yoon–Nelson model is suitable for adequately describing the dynamic adsorption of NO_3^- in groundwater on the pristine and modified biochar materials (Golie and Upadhyayula, 2016).

3.5 Possible NO_3^- removal mechanism

The FTIR spectra of ECL, La–ECL, and La/CTAC–ECL before and after NO_3^- adsorption was highly similar (Figure 3C). After ECL, La–ECL, and La/CTAC–EC adsorbed NO_3^-, the intensity of the infrared characteristic peaks especially at 3,201–3,340 cm^{-1} and 2,923 cm^{-1} was significantly reduced. This result might be attributed to the hydrogen bond between the H of O–H and –CH_2 groups on their surfaces the O on nitrate, thereby adsorbing nitrate (Teng et al., 2022). Therefore, hydrogen bonds may be a key mechanism to control nitrate adsorption efficiency. Moreover, the weakened tensile vibration peak after NO_3^- adsorption also confirmed the ion exchange between the negative charge of groups derived from biochar and NO_3^-.

The C 1 s spectrum, N 1 s spectrum, O 1 s spectrum, and La 3 d spectra of ECL, La–ECL, and La/CTAC–ECL before and after nitrate adsorption were shown in Supplementary Figure S2, Figure 8, respectively. The intensity of O 1s peak of ECL, La–ECL, and La/CTAC–ECL declined dramatically in the wide scan XPS spectrum (Figure 3D), which demonstrated the involvement of the O–containing functional groups (M–O) of biochar in NO_3^- adsorption. The main peak of N 1s on the sample of ECL, La–ECL, and La/CTAC–ECL could be divided into

Three characteristic peaks at 398.42, 399.82, and 400.77 eV (Supplementary Figure S2), which were assigned to sp2–hybridized N (–N=C–), benzene amine (–NH_2– or –NH–) and ternary N (N–C_3) groups, respectively. The percentage of benzene amine (–NH_2– or –NH–) in the ECL, La–ECL, and La/CTAC–ECL after NO_3^- adsorption declined (Figure 8), suggesting that nitrate was removed from the aqueous solution by electrostatic attraction (Wang et al., 2022). Additionally, the N 1s binding energy of the N–O in the La/CTAC–ECL decreased by 0.31 eV after NO_3^- adsorption (Supplementary Figure S2, Figure 8), indicating that a chemical bond may be formed between NO_3^- and CTAC.

According to the La 3d scan (Supplementary Figure S2), on the surface of La–ECL and La/CTAC–ECL, the characteristic peaks of La 3d3/2 were spliced into two dominant peaks at binding energies of 856.11 and 852.86 eV, while the binding energies of 839.16 and 835.86 eV were attributed to the peaks of La 3d5/2 (Li et al., 2020). After NO_3^- was adsorbed, the binding energies on the surface of La–ECL and La/CTAC–ECL had a slight shifted by + 0.39 eV, + 0.65 eV at La 3d3/2 and + 0.31 eV, + 0.52 eV at La 3d5/2 (Figure 8). The above–mentioned results suggested the valence electron transfer of La 3 d existed, and an inner sphere La–O–N complexations were formed on the surface of La–ECL and La/CTAC–ECL (Zhang et al., 2021).

4 Conclusion

In the present study, the breakthrough time for NO_3^- in a simulated PRB column increased as the initial NO_3^- concentration of the influent increased and the flow rate decreased, whereas with the increase of filler particle size and the height of the filler in the column initially increased, and then decreased. Considering an initial NO_3^- concentration of 50 mg L^{-1}, and filler particle size range of 0.8–1.2 mm, the maximum adsorption capacity of the La/CTAC–ECL column for NO_3^- is 18.99 mg g^{-1} for a filler column height of 10 cm and an influent flow rate of 15 ml min^{-1}. Simultaneously, the maximum quantity of adsorbed NO_3^- of 372.80 mg is obtained using a filler column height of 15 cm and an influent flow rate of 10 ml min^{-1}.

The Thomas and Yoon–Nelson models were utilized to accurately predict the breakthrough process of NO_3^- in groundwater in a simulated PRB column under different conditions, and the results were consistent with those from dynamic adsorption experiments. Characterization of the materials using TEM, XRD, FTIR, and XPS showed that the modification using both La and CTAC improved the structure of the surface of the pristine biochar by optimizing the configuration of functional groups and enhancing its porosity and permeability coefficient. These changes revealed that mechanisms of NO_3^- removal from groundwater using the La/CTAC–ECL comprised pore filling, surface adsorption, ion exchange, and electrostatic adsorption. The La/CTAC–ECL biochar composite exhibited a significant potential for the remediation of NO_3^- contaminated groundwater. Therefore, the production of biochar from the *Erigeron canadensis* L. for the treatment of contaminated water can help to preserve biodiversity and the environment in areas in which it is invasive.

Data availability statement

The original contributions presented in the study are included in the article/Supplementary Material, further inquiries can be directed to the corresponding authors.

Author contributions

SL: investigation, formal analysis, methodology, and writing–original draft. YW: conceptualization, methodology, and writing–reviewing. FN, XLi, HF and TS: data curation, validation, formal analysis, and writing–original draft. WT, YL and XLu: investigation, supervision, and resources. All authors have read and agreed to the published version of the manuscript.

Funding

This work was financially supported by the Science and Technology Key Research Support Foundation of Sichuan Province (2018SZ0311, 2021YFN0128, 2021YFQ0067, 2022YFS0475, and 2022YFS0498).

Acknowledgments

We thank Hongtao Li and Qin Liu for helping in the field work and lab experiment. We also sincerely thank Editage (https://www.editage.cn) for editing the language of a draft of this manuscript.

Conflict of interest

The authors declare that the research was conducted in the absence of any commercial or financial relationships that could be construed as a potential conflict of interest.

Publisher's note

Supplementary material

The Supplementary Material for this article can be found online at: https://www.frontiersin.org/articles/10.3389/fenvs.2022.986866/full#supplementary-material

References

Alsewaileh, A. S., Usman, A. R., and Al-Wabel, M. I. (2019). Effects of pyrolysis temperature on nitrate-nitrogen (NO_3^--N) and bromate (BrO_3^-) adsorption onto date palm biochar. *J. Environ. Manage.* 237, 289–296. doi:10.1016/j.jenvman.2019.02.045

Ambaye, T. G., Vaccari, M., van Hullebusch, E. D., Amrane, A., and Rtimi, S. (2021). Mechanisms and adsorption capacities of biochar for the removal of organic and inorganic pollutants from industrial wastewater. *Int. J. Environ. Sci. Technol. (Tehran).* 18, 3273–3294. doi:10.1007/s13762-020-03060-w

Amoako-Nimako, G. K., Yang, X., and Chen, F. (2021). Denitrification using permeable reactive barriers with organic substrate or zero-valent iron fillers: controlling mechanisms, challenges, and future perspectives. *Environ. Sci. Pollut. Res.* 28, 21045–21064. doi:10.1007/s11356-021-13260-7

Anshumala, K., Shukla, J. P., Patel, S. S., and Singh, A. (2021). Assessment of groundwater vulnerability zone in mandideep industrial area using DRASTIC model. *J. Geol. Soc. India* 97, 1080–1086. doi:10.1007/s12594-021-1823-y

Aytas, S., Yurtlu, M., and Donat, R. (2009). Adsorption characteristic of U(VI) ion onto thermally activated bentonite. *J. Hazard. Mat.* 172, 667–674. doi:10.1016/j.jhazmat.2009.07.049

Chakraborty, A., Suchy, M., Hubert, C. R. J., and Ryan, M. C. (2022). Vertical stratification of microbial communities and isotope geochemistry tie groundwater denitrification to sampling location within a nitrate-contaminated aquifer. *Sci. Total Environ.* 820, 153092. doi:10.1016/j.scitotenv.2022.153092

Chandra, S., Medha, I., and Bhattacharya, J. (2020). Potassium-iron rice straw biochar composite for sorption of nitrate, phosphate, and ammonium ions in soil for timely and controlled release. *Sci. Total Environ.* 712, 136337. doi:10.1016/j.scitotenv.2019.136337

Dai, Y., Wang, W., Lu, L., Yan, L., and Yu, D. (2020). Utilization of biochar for the removal of nitrogen and phosphorus. *J. Clean. Prod.* 257, 120573. doi:10.1016/j.jclepro.2020.120573

Dai, Y., Zhang, N., Xing, C., Cui, Q., and Sun, Q. (2019). The adsorption, regeneration and engineering applications of biochar for removal organic pollutants: a review. *Chemosphere* 223, 12–27. doi:10.1016/j.chemosphere.2019.01.161

de Repentigny, C., Courcelles, B., and Zagury, G. J. (2018). Spent MgO-carbon refractory bricks as a material for permeable reactive barriers to treat a nickel- and cobalt-contaminated groundwater. *Environ. Sci. Pollut. Res.* 25, 23205–23214. doi:10.1007/s11356-018-2414-3

Faisal, A. A. H., Al-Wakel, S. F. A., Assi, H. A., Naji, L. A., and Naushad, M. (2020). Waterworks sludge-filter sand permeable reactive barrier for removal of toxic lead ions from contaminated groundwater. *J. Water Process Eng.* 33, 101112. doi:10.1016/j.jwpe.2019.101112

Fu, X., Hou, R., Yang, P., Qian, S., Feng, Z., Chen, Z., et al. (2022). Application of external carbon source in heterotrophic denitrification of domestic sewage: a review. *Sci. Total Environ.* 817, 153061. doi:10.1016/j.scitotenv.2022.153061

Fu, Y., Wang, F., Sheng, H., Hu, F., Wang, Z., Xu, M., et al. (2021). Removal of extracellular antibiotic resistance genes using magnetic biochar/quaternary phosphonium salt in aquatic environments: a mechanistic study. *J. Hazard. Mat.* 411, 125048. doi:10.1016/j.jhazmat.2021.125048

Gao, J., Zhai, Y., Huang, Z., Ren, P., Gao, J., Chen, Z., et al. (2021). Remediation of Cr(VI)/Cd(II)-Contaminated groundwater with simulated permeable reaction barriers filled with composite of sodium dodecyl benzene sulfonate-modified maifanite and anhydride-modified Fe@SiO_2@Polyethyleneimine: Environmental factors and effectiveness. *Adsorp. Sci. Technol.* 2021, 1–19. doi:10.1155/2021/4998706

Ghaeminia, M., and Mokhtarani, N. (2018). Remediation of nitrate-contaminated groundwater by PRB-Electrokinetic integrated process. *J. Environ. Manage.* 222, 234–241. doi:10.1016/j.jenvman.2018.05.078

Gibert, O., Assal, A., Devlin, H., Elliot, T., and Kalin, R. M. (2019). Performance of a field-scale biological permeable reactive barrier for *in-situ* remediation of nitrate-contaminated groundwater. *Sci. Total Environ.* 659, 211–220. doi:10.1016/j.scitotenv.2018.12.340

Gizaw, A., Zewge, F., Chebude, Y., Mekonnen, A., and Tesfaye, M. (2022). Simultaneous nitrate and phosphate abatement using calcium silicate hydrate adsorbent: Fixed bed column adsorption study. *Surfaces Interfaces* 30, 101961. doi:10.1016/j.surfin.2022.101961

Golie, W. M., and Upadhyayula, S. (2016). Continuous fixed-bed column study for the removal of nitrate from water using chitosan/alumina composite. *J. Water Process Eng.* 12, 58–65. doi:10.1016/j.jwpe.2016.06.007

Guo, C., Qi, L., Bai, Y., Yin, L., Li, L., and Zhang, W. (2021). Geochemical stability of zero-valent iron modified raw wheat straw innovatively applicated to *in situ* permeable reactive barrier: N_2 selectivity and long-term denitrification. *Ecotoxicol. Environ. Saf.* 224, 112649. doi:10.1016/j.ecoenv.2021.112649

Gupta, S., and Kua, H. W. (2019). Carbonaceous micro-filler for cement: Effect of particle size and dosage of biochar on fresh and hardened properties of cement mortar. *Sci. Total Environ.* 662, 952–962. doi:10.1016/j.scitotenv.2019.01.269

Haque, M. I., Khan, R. I., Ashraf, W., and Pendse, H. (2021). Production of sustainable, low-permeable and self-sensing cementitious composites using biochar. *Sustain. Mater. Technol.* 28, e00279. doi:10.1016/j.susmat.2021.e00279

Hasan, M. S., Geza, M., Vasquez, R., Chilkoor, G., and Gadhamshetty, V. (2020). Enhanced heavy metal removal from synthetic stormwater using nanoscale zerovalent iron–modified biochar. *Water Air Soil Pollut.* 231, 220. doi:10.1007/s11270-020-04588-w

He, S., Li, P., Su, F., Wang, D., and Ren, X. (2022). Identification and apportionment of shallow groundwater nitrate pollution in Weining Plain, northwest China, using hydrochemical indices, nitrate stable isotopes, and the new Bayesian stable isotope mixing model (MixSIAR). *Environ. Pollut.* 298, 118852. doi:10.1016/j.envpol.2022.118852

Jia, X., O'Connor, D., Hou, D., Jin, Y., Li, G., Zheng, C., et al. (2019). Groundwater depletion and contamination: Spatial distribution of groundwater resources sustainability in China. *Sci. Total Environ.* 672, 551–562. doi:10.1016/j.scitotenv.2019.03.457

Kim, H., Yu, S., Oh, J., Kim, K., Lee, J., Moniruzzaman, M., et al. (2019). Nitrate contamination and subsequent hydrogeochemical processes of shallow groundwater in agro-livestock farming districts in South Korea. *Agric. Ecosyst. Environ.* 273, 50–61. doi:10.1016/j.agee.2018.12.010

Kong, L., Tian, Y., Pang, Z., Huang, X., Li, M., Yang, R., et al. (2019). Synchronous phosphate and fluoride removal from water by 3D rice-like lanthanum-doped La@MgAl nanocomposites. *Chem. Eng. J.* 371, 893–902. doi:10.1016/j.cej.2019.04.116

Kosaiyakanon, C., and Kungsanant, S.Department of Chemical Engineering, Faculty of Engineering, Prince of Songkla University, Hat-Yai, Songkhla 90110, Thailand (2020). Adsorption of reactive dyes from wastewater using cationic surfactant-modified coffee husk biochar. *Environ. Nat. Resour. J.* 18, 21–32. doi:10.32526/ennrj.18.1.2020.03

Krimsky, L. S., Lusk, M. G., Abeels, H., and Seals, L. (2021). Sources and concentrations of nutrients in surface runoff from waterfront homes with different landscape practices. *Sci. Total Environ.* 750, 142320. doi:10.1016/j.scitotenv.2020.142320

Kumari, K., Swain, A. A., Kumar, M., and Bauddh, K. (2021). Utilization of *Eichhornia crassipes* biomass for production of biochar and its feasibility in agroecosystems: a review. *Environ. Sustain.* 4, 285–297. doi:10.1007/s42398-021-00185-7

Lakshmi, D., Akhil, D., Kartik, A., Gopinath, K. P., Arun, J., Bhatnagar, A., et al. (2021). Artificial intelligence (AI) applications in adsorption of heavy metals using modified biochar. *Sci. Total Environ.* 801, 149623. doi:10.1016/j.scitotenv.2021.149623

Li, J., Li, B., Huang, H., Zhao, N., Zhang, M., and Cao, L. (2020). Investigation into lanthanum-coated biochar obtained from urban dewatered sewage sludge for enhanced phosphate adsorption. *Sci. Total Environ.* 714, 136839. doi:10.1016/j.scitotenv.2020.136839

Li, Y., Zhang, F., Yang, M., Zhang, J., and Xie, Y. (2019). Impacts of biochar application rates and particle sizes on runoff and soil loss in small cultivated loess plots under simulated rainfall. *Sci. Total Environ.* 649, 1403–1413. doi:10.1016/j.scitotenv.2018.08.415

Lim, A. P., and Aris, A. Z. (2014). Continuous fixed-bed column study and adsorption modeling: removal of cadmium (II) and lead (II) ions in aqueous solution by dead calcareous skeletons. *Biochem. Eng. J.* 87, 50–61. doi:10.1016/j.bej.2014.03.019

Liu, D., Yang, L., Wu, J., and Li, B. (2022). Molten salt shielded preparation of rice straw biochars doped by copper sulfide for elemental mercury capture. *J. Energy Inst.* 102, 176–183. doi:10.1016/j.joei.2022.03.005

Liu, M., Xiao, C., Liang, X., and Wei, H. (2022). Response of groundwater chemical characteristics to land use types and health risk assessment of nitrate in semi-arid areas: a case study of shuangliao city, northeast China. *Ecotoxicol. Environ. Saf.* 236, 113473. doi:10.1016/j.ecoenv.2022.113473

Luo, W., Huang, Q., Zhang, X., Antwi, P., Mu, Y., Zhang, M., et al. (2020). Lanthanum/Gemini surfactant-modified montmorillonite for simultaneous removal of phosphate and nitrate from aqueous solution. *J. Water Process Eng.* 33, 101036. doi:10.1016/j.jwpe.2019.101036

Mahendra, C., Sathya Sai, P. M., Anand Babu, C., Revathy, K., and Rajan, K. K. (2015). Analysis and modeling of fixed bed sorption of cesium by AMP-PAN. *J. Environ. Chem. Eng.* 3, 1546–1554. doi:10.1016/j.jece.2015.05.002

McDonough, L. K., Santos, I. R., Andersen, M. S., O Carroll, D. M., Rutlidge, H., Meredith, K., et al. (2020). Changes in global groundwater organic carbon driven by climate change and urbanization. *Nat. Commun.* 11, 1279. doi:10.1038/s41467-020-14946-1

Mittal, A., Singh, R., Chakma, S., and Goel, G. (2020). Permeable reactive barrier technology for the remediation of groundwater contaminated with nitrate and phosphate resulted from pit-toilet leachate. *J. Water Process Eng.* 37, 101471. doi:10.1016/j.jwpe.2020.101471

Qiu, B., Tao, X., Wang, H., Li, W., Ding, X., and Chu, H. (2021). Biochar as a low-cost adsorbent for aqueous heavy metal removal: A review. *J. Anal. Appl. Pyrolysis* 155, 105081. doi:10.1016/j.jaap.2021.105081

Qu, J., Akindolie, M. S., Feng, Y., Jiang, Z., Zhang, G., Jiang, Q., et al. (2020). One-pot hydrothermal synthesis of $NaLa(CO_3)_2$ decorated magnetic biochar for efficient phosphate removal from water: Kinetics, isotherms, thermodynamics, mechanisms and reusability exploration. *Chem. Eng. J.* 394, 124915. doi:10.1016/j.cej.2020.124915

Ramírez-Rodríguez, A. E., Morales-Barrera, L., and Cristiani-Urbina, E. (2021). Continuous biosorption of acid red 27 azo dye by *Eichhornia crassipes* leaves in a packed-bed column. *Sci. Rep.* 11, 18413. doi:10.1038/s41598-021-98034-4

Setshedi, K. Z., Bhaumik, M., Onyango, M. S., and Maity, A. (2014). Breakthrough studies for Cr(VI) sorption from aqueous solution using exfoliated polypyrrole-organically modified montmorillonite clay nanocomposite. *J. Ind. Eng. Chem.* 20, 2208–2216. doi:10.1016/j.jiec.2013.09.052

Shahverdi, M., Kouhgardi, E., and Ramavandi, B. (2016). Characterization, kinetic, and isotherm data for Cr (VI) removal from aqueous solution by Populus alba biochar modified by a cationic surfactant. *Data Brief* 9, 163–168. doi:10.1016/j.dib.2016.08.051

Shaji, E., Santosh, M., Sarath, K. V., Prakash, P., Deepchand, V., and Divya, B. V. (2021). Arsenic contamination of groundwater: a global synopsis with focus on the Indian peninsula. *Geosci. Front.* 12, 101079. doi:10.1016/j.gsf.2020.08.015

Song, J., Huang, G., Han, D., Hou, Q., Gan, L., and Zhang, M. (2021). A review of reactive media within permeable reactive barriers for the removal of heavy metal(loid)s in groundwater: Current status and future prospects. *J. Clean. Prod.* 319, 128644. doi:10.1016/j.jclepro.2021.128644

Spalding, R. F., Hirsh, A. J., Exner, M. E., Little, N. A., and Kloppenborg, K. L. (2019). Applicability of the dual isotopes δ15N and δ18O to identify nitrate in groundwater beneath irrigated cropland. *J. Contam. Hydrol.* 220, 128–135. doi:10.1016/j.jconhyd.2018.12.004

Stayner, L. T., Schullehner, J., Semark, B. D., Jensen, A. S., Trabjerg, B. B., Pedersen, M., et al. (2021). Exposure to nitrate from drinking water and the risk of childhood cancer in Denmark. *Environ. Int.* 155, 106613. doi:10.1016/j.envint.2021.106613

Taufiq, A., Effendi, A. J., Iskandar, I., Hosono, T., and Hutasoit, L. M. (2019). Controlling factors and driving mechanisms of nitrate contamination in groundwater system of Bandung Basin, Indonesia, deduced by combined use of stable isotope ratios, CFC age dating, and socioeconomic parameters. *Water Res.* 148, 292–305. doi:10.1016/j.watres.2018.10.049

Temkin, A., Evans, S., Manidis, T., Campbell, C., and Naidenko, O. V. (2019). Exposure-based assessment and economic valuation of adverse birth outcomes and cancer risk due to nitrate in United States drinking water. *Environ. Res.* 176, 108442. doi:10.1016/j.envres.2019.04.009

Teng, Y., Song, G., Chen, R., Zhang, X., Sun, Y., Wu, H., et al. (2022). Carboxymethyl β-cyclodextrin immobilized on hydrated lanthanum oxide for simultaneous adsorption of nitrate and phosphate. *J. Taiwan Inst. Chem. Eng.* 132, 104153. doi:10.1016/j.jtice.2021.11.020

USEPA (2012). *2012 edition of the drinking water standards and health advisories*. Washington, DC, USA.

Usman, A. R. A., Ahmad, M., El-Mahrouky, M., Al-Omran, A., Ok, Y. S., Sallam, A. S., et al. (2016). Chemically modified biochar produced from conocarpus waste increases NO_3 removal from aqueous solutions. *Environ. Geochem. Health* 38, 511–521. doi:10.1007/s10653-015-9736-6

Velusamy, K., Periyasamy, S., Kumar, P. S., Vo, D. N., Sindhu, J., Sneka, D., et al. (2021). Advanced techniques to remove phosphates and nitrates from waters: a review. *Environ. Chem. Lett.* 19, 3165–3180. doi:10.1007/s10311-021-01239-2

Vijayaraghavan, K., and Balasubramanian, R. (2021). Application of pinewood waste-derived biochar for the removal of nitrate and phosphate from single and binary solutions. *Chemosphere* 278, 130361. doi:10.1016/j.chemosphere.2021.130361

Vilvanathan, S., and Shanthakumar, S. (2017). Column adsorption studies on nickel and cobalt removal from aqueous solution using native and biochar form of Tectona grandis. *Environ. Prog. Sustain. Energy* 36, 1030–1038. doi:10.1002/ep.12567

Wang, H., Liu, R., Chen, Q., Mo, Y., and Zhang, Y. (2022). Biochar-supported starch/chitosan-stabilized nano-iron sulfide composites for the removal of lead ions and nitrogen from aqueous solutions. *Bioresour. Technol.* 347, 126700. doi:10.1016/j.biortech.2022.126700

Wang, Z., Shen, D., Shen, F., and Li, T. (2016). Phosphate adsorption on lanthanum loaded biochar. *Chemosphere* 150, 1–7. doi:10.1016/j.chemosphere.2016.02.004

Wu, R. S. S., Lam, K. H., Lee, J. M. N., and Lau, T. C. (2007). Removal of phosphate from water by a highly selective La(III)-chelex resin. *Chemosphere* 69, 289–294. doi:10.1016/j.chemosphere.2007.04.022

Yan, L., Liu, Y., Zhang, Y., Liu, S., Wang, C., Chen, W., et al. (2020). $ZnCl_2$ modified biochar derived from aerobic granular sludge for developed microporosity and enhanced adsorption to tetracycline. *Bioresour. Technol.* 297, 122381. doi:10.1016/j.biortech.2019.122381

Yang, J., Li, H., Zhang, D., Wu, M., and Pan, B. (2017). Limited role of biochars in nitrogen fixation through nitrate adsorption. *Sci. Total Environ.* 592, 758–765. doi:10.1016/j.scitotenv.2016.10.182

Yang, Z., Zhou, Y., Feng, Z., Rui, X., Zhang, T., and Zhang, Z. (2019). A review on reverse osmosis and nanofiltration membranes for water purification. *Polym. (Basel).* 11, 1252. doi:10.3390/polym11081252

Yuan, C., Wang, Q., Chen, Y., Zhang, L., Tan, L., Fu, R., et al. (2021). Impacts of a biocontrol agent on invasive Ageratina adenophora in Southwest China: Friend or foe? *Biol. Control* 152, 104471. doi:10.1016/j.biocontrol.2020.104471

Zhang, M., Song, G., Gelardi, D. L., Huang, L., Khan, E., Mašek, O., et al. (2020). Evaluating biochar and its modifications for the removal of ammonium, nitrate, and phosphate in water. *Water Res.* 186, 116303. doi:10.1016/j.watres.2020.116303

Zhang, T., Tu, Z., Lu, G., Duan, X., Yi, X., Guo, C., et al. (2017). Removal of heavy metals from acid mine drainage using chicken eggshells in column mode. *J. Environ. Manage.* 188, 1–8. doi:10.1016/j.jenvman.2016.11.076

Zhang, Y., Akindolie, M. S., Tian, X., Wu, B., Hu, Q., Jiang, Z., et al. (2021). Enhanced phosphate scavenging with effective recovery by magnetic porous biochar supported $La(OH)_3$: kinetics, isotherms, mechanisms and applications for water and real wastewater. *Bioresour. Technol.* 319, 124232. doi:10.1016/j.biortech.2020.124232

Zhao, B., Sun, Z., and Liu, Y. (2022). An overview of *in-situ* remediation for nitrate in groundwater. *Sci. Total Environ.* 804, 149981. doi:10.1016/j.scitotenv.2021.149981

Zhao, H., Xue, Y., Long, L., and Hu, X. (2018). Adsorption of nitrate onto biochar derived from agricultural residuals. *Water Sci. Technol.* 77, 548–554. doi:10.2166/wst.2017.568

Zheng, Z., Ali, A., Su, J., Fan, Y., and Zhang, S. (2021). Layered double hydroxide modified biochar combined with sodium alginate: a powerful biomaterial for enhancing bioreactor performance to remove nitrate. *Bioresour. Technol.* 323, 124630. doi:10.1016/j.biortech.2020.124630

Zhi, Y., Paterson, A. R., Call, D. F., Jones, J. L., Hesterberg, D., Duckworth, O. W., et al. (2022). Mechanisms of orthophosphate removal from water by lanthanum carbonate and other lanthanum-containing materials. *Sci. Total Environ.* 820, 153153. doi:10.1016/j.scitotenv.2022.153153

Zhou, Y., Xiao, J., Hu, R., Wang, T., Shao, X., Chen, G., et al. (2020). Engineered phosphorous-functionalized biochar with enhanced porosity using phytic acid-assisted ball milling for efficient and selective uptake of aquatic uranium. *J. Mol. Liq.* 303, 112659. doi:10.1016/j.molliq.2020.112659